

Electrostatically defined few-electron double quantum dot in silicon

W.H. Lim, H. Huebl, L.H. Willems van Beveren, R.G. Clark, and A.S. Dzurak
*Australian Research Council Centre of Excellence for Quantum Computer Technology,
 The University of New South Wales, Sydney 2052, Australia*

S. Rubanov, P.G. Spizzirri, and S.J. Angus
*Australian Research Council Centre of Excellence for Quantum Computer Technology,
 The University of Melbourne, Victoria 3010, Australia*

(Dated: February 21, 2024)

A few-electron double quantum dot was fabricated using metal-oxide-semiconductor (MOS)-compatible technology and low-temperature transport measurements were performed to study the energy spectrum of the device. The double dot structure is electrically tunable, enabling the inter-dot coupling to be adjusted over a wide range, as observed in the charge stability diagram. Resonant single-electron tunneling through ground and excited states of the double dot was clearly observed in bias spectroscopy measurements.

Keywords: double quantum dot, FastCap, XTEM, silicon

Electrostatically defined single and double quantum dot (DQD) systems in GaAs/AlGaAs heterostructures [1, 2] are the current benchmark for the implementation of DiVincenzo's criteria using semiconductor qubits [3, 4, 5]. Although the nuclear spins inherently present in GaAs provide a fast decoherence mechanism, this drawback has been partly overcome recently [6]. Silicon has a natural advantage in this respect since the only stable isotope with a nuclear spin is ^{29}Si . The 4.7% abundance of this isotope in $^{\text{nat}}\text{Si}$ can be reduced by isotopic purification, resulting in nearly nuclear-spin-free crystals. This should, in principle, increase the coherence time of electron-spin qubits in silicon [7, 8]. Initial demonstrations of Si-based DQD systems for spin qubits [9, 10] have stimulated a number of recent studies of DQDs in both multi-gated silicon-on-insulator (SOI) [11, 12] and Si/SiGe [13] structures.

In this letter, we report the fabrication of a few-electron DQD and its electrical measurement at millikelvin temperatures. The double dot is based upon a recently developed double-gated silicon quantum dot [14], which was also shown to operate effectively as a radio-frequency single electron transistor [15]. Our approach provides a simple method of producing multi-gated silicon quantum dots without the need for complementary-MOS (CMOS) process technologies, such as polysilicon deposition and etching. The morphology of the double dot device is investigated using cross-sectional transmission electron microscopy (XTEM) analysis. Transport spectroscopy demonstrates the ability to tune the double dot from the weakly-coupled to strongly-coupled regime. In the weakly-coupled regime, extracted capacitances of the system show good quantitative agreement with simple modelling using FastCap [16].

The devices investigated in this work were fabricated on near-intrinsic silicon wafers ($\rho > 10 \text{ k}\Omega\cdot\text{cm}$ at 300 K). After definition of n^+ ohmic contacts by phosphorus diffusion through a masked sacrificial thermal oxide, a

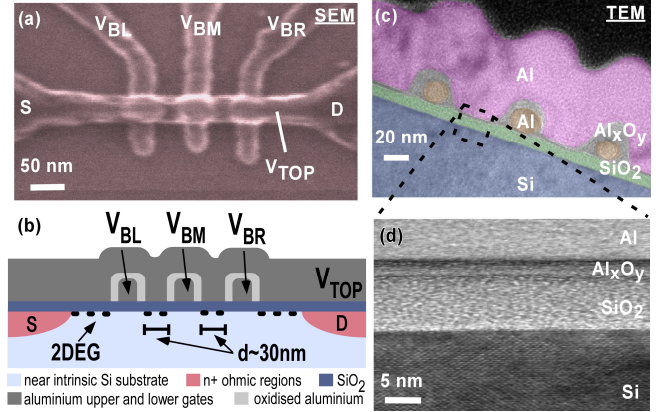


FIG. 1: (a) SEM image of the Si MOS DQD. The three barrier gates and the top gate have widths $\sim 30 \text{ nm}$ and $\sim 50 \text{ nm}$ respectively. The Al barrier gates were plasma-oxidized to isolate them from the top gate. (b) Schematic cross-section of the device (not to scale). Source and drain n^+ contacts (red) were formed by phosphorus diffusion into the Si substrate (light blue). The top gate induces a 2DEG and the barrier gates create three potential barriers, forming two dots. The size of the dots is estimated to be $30 \times 50 \text{ nm}^2$. (c) Color-enhanced XTEM image of a similar device. (d) Enlarged XTEM image, showing sharp interfaces between the Si substrate, SiO_2 gate oxide, Al_xO_y and the Al top gate.

200 nm field oxide was grown. In the active device region ($30 \times 30 \mu\text{m}^2$), the field oxide was etched locally and replaced by an 8 nm-thick high-quality SiO_2 gate oxide, grown in an ultra-dry oxidation furnace at $800 \text{ }^\circ\text{C}$ in O_2 and dichloroethylene. Three Al barrier gates were then patterned by electron beam lithography (EBL), thermal evaporation and lift-off. The barrier gates were next passivated by plasma oxidation [14, 17], resulting in an electrically-insulating Al_xO_y layer surrounding the barrier gates. The Al top gate was defined in a second EBL step aligned to the lower gates with an accuracy

of ~ 20 nm. Finally, the devices were annealed at 400 °C for 15 mins in forming gas (95% N_2 /5% H_2) to reduce the Si/SiO₂ interface trap density (D_{it}). Deep-level transient spectroscopy of similarly-processed structures revealed D_{it} of order 5×10^{10} cm⁻²eV⁻¹ near the conduction band edge [18].

Figures 1(a,b) show a scanning electron microscope (SEM) image and a schematic cross-section of a double dot device. The top gate, which extends over the source and drain n⁺ contacts (not shown) and also the three barrier gates are used to form a two-dimensional electron gas (2DEG) accumulation layer under the thin SiO₂ layer. The barrier gates are used to locally deplete the 2DEG, forming three tunnel barriers that define two dots in series. The dots are geometrically defined by the distance between adjacent barrier gates (~ 30 nm), and by the top gate width (~ 50 nm). The outer barrier gates and top gate are used to control the electron occupancies electrostatically and the middle barrier gate is used to control the inter-dot coupling.

Figure 1(c) shows an XTEM image along the top gate (i.e. perpendicular to the barrier gates). Apart from an increased (200 nm) top-gate width in order to aid XTEM sample preparation, this device is nominally identical to the device used in electrical measurements. The XTEM image confirms the target 5 nm Al_xO_y layer thickness from the plasma oxidation process used (100 mTorr, 50 W incident RF O₂ plasma, 150 °C for 3 mins). Interestingly, at the interface between the top gate and the SiO₂, we find an additional Al_xO_y layer (~ 2 nm thick, see Fig. 1(d)) which could be due to the oxidation of the Al top gate via chemical interaction with the SiO₂ layer below. We note that the Al barrier gates, initially evaporated to a thickness of 30 nm, show an Al core of only ~ 20 nm in diameter after plasma oxidation, consistent with the formation of a ~ 5 nm Al_xO_y insulator. This Al_xO_y thickness is sufficient to allow differential biases of up to 4 V between the upper and lower gates with negligible leakage.

Electrical (dc) transport measurements were performed in an Oxford Instruments Kelvinox K100 dilution refrigerator at a base temperature of ~ 50 mK. A source-drain excitation voltage $V_{sd} = 50$ μ V at a modulation frequency of 13 Hz was used to monitor the differential conductance dI/dV_{sd} . The source-drain dc current I_{SD} was measured with a room-temperature current preamplifier. Initially, the left (right) dot was characterized independently by setting the right (left) barrier-gate voltage $V_{BR}(V_{BL})$ equal to the top gate voltage V_{TOP} . The middle barrier gate voltage V_{BM} was fixed at $V_{BM} = 0.818$ V. Under these conditions Coulomb diamonds were recorded and the charging energy of the left (right) dot, was determined to be $E_C \sim 5$ meV (~ 2.5 meV) at $V_{TOP} = 1.6$ V. Therefore, the total capacitance of the left (right) dot was $C_{\Sigma, left(right)} = e^2/E_C \sim 30$ aF (~ 60 aF) at $V_{BL} = 0.76$ V ($V_{BR} = 0.76$ V). To compare these experimentally ob-

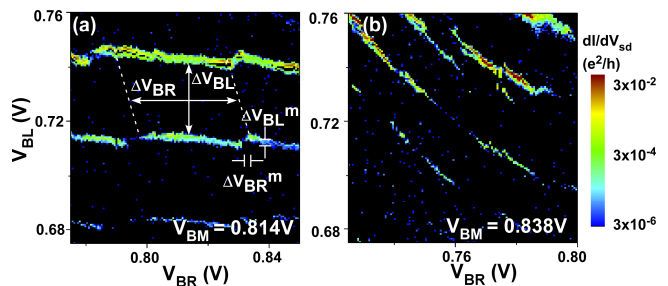


FIG. 2: Differential conductance dI/dV_{sd} as a function of the barrier gate voltages, V_{BL} and V_{BR} , for $V_{TOP} = 1.6$ V and zero source-drain bias. Tuning the middle gate voltage in the range $V_{BM} = 0.814$ V – 0.830 V, we observe a transition from two almost isolated dots (a) to the formation of a single large dot (b).

tained results with modelled parameters, we used Fast-Cap which calculates the capacitances based on a finite element approach. Using the lithographic device dimensions as inputs, we obtained a total capacitance $C_{\Sigma} \sim 30$ aF for both dots, in good agreement with the experimental value for the left dot but at variance with that of the right dot by a factor of two. Such variations in capacitance from dot to dot could result from physical asymmetries in real devices, as evidenced by the XTEM image in Fig. 1(c), or from the presence of fixed charge in the gate oxide or at interfaces which can modify the effective gate potentials.

We estimate the electron occupancy of a single dot using two methods. The first method uses Hall measurements of a similar MOSFET device from which the electron density is determined to be $n = 3.5 \times (V_{TOP} - V_{TH})10^{12}$ cm⁻² [19], where V_{TH} is the threshold voltage. When operated as a simple MOSFET, our device showed $V_{TH} \sim 1.25$ V. Hence, at $V_{TOP} = 1.6$ V we estimate the 2DEG density of our device to be $n \sim 1.2 \times 10^{12}$ cm⁻², resulting in a dot occupancy of $N \sim 20$ electrons for a 30×50 nm dot size. As an alternative method, we estimate electron occupancy by counting Coulomb oscillations from V_{TH} , assuming no free electrons in the dots below threshold voltage [14]. This method derives a dot occupancy of $N \sim 15$, in reasonable agreement with the previous method. Both approaches indicate that the device operates in the few electron regime.

Figure 2 shows the differential conductance dI/dV_{sd} of the DQD as a function of the barrier-gate voltages, V_{BL} and V_{BR} , for a fixed top-gate voltage $V_{TOP} = 1.6$ V and source drain voltage $V_{SD} = 0$ V for two different middle barrier-gate voltages V_{BM} . In Fig. 2(a), the relatively low middle barrier-gate voltage $V_{BM} = 0.814$ V and therefore high central barrier separates the two dots, resulting in the characteristic honeycomb-shaped charge stability diagram. By calculating the voltage ratios $\Delta V_{BR}^m / \Delta V_{BR}$ ($\Delta V_{BL}^m / \Delta V_{BL}$), we can estimate the ratios of the mutual capacitance to the total dot capacitance

$C_m/C_{\Sigma, \text{left(right)}} \sim 0.10(0.07)$, indicating that the double dot is in the weak coupling regime [2]. There, we observe the characteristic triple points resulting from the alignment of the electrochemical potentials of the dots and the leads. In addition, current is observed along the sides of the hexagons, which can occur when the dots are strongly coupled to the leads and second-order co-tunneling processes occur [20]. Increasing the middle barrier gate voltage to $V_{BM}=0.838$ V, the mutual capacitance increases and dominates the system ($C_m/C_{\Sigma, \text{left(right)}} \sim 1$). This situation occurs when the middle barrier is reduced and a single (merged) large dot is formed, resulting in diagonal parallel Coulomb lines, as observed in Fig. 2(b).

Figure 3(a) shows transport data through the DQD in the weak coupling regime $V_{BM}=0.802$ V with $V_{TOP}=1.4$ V and $V_{SD}=-1.0$ mV. For $|V_{SD}| > 0$ the triple points evolve into so-called bias triangles, reflecting the occurrence of transport within the bias windows [2]. In a double dot system, two types of coupling can be distinguished: capacitive coupling; and tunnel coupling. While capacitive coupling is a purely classical effect, tunnel coupling arises from the overlap of electron wave functions, classified by the fractional splitting ratio $F = 2\Delta V_s/V_p$, where ΔV_s is the splitting between the paired triangles and ΔV_p is the diagonal separation between triangle pairs in Fig. 3(a) [21, 22]. Here, we find $F \sim 0.2$, indicating that the interaction between the two dots is dominated by capacitive coupling. The device may therefore be modelled using a capacitive approach.

From the dimensions of the hexagon and triangles in Fig. 3(a) we obtain the key capacitances defining the system [2], namely: the total capacitances of the left and right dots, $C_{\Sigma, \text{left(right)}}$; the mutual capacitance between the two dots, C_m ; the relative capacitances between each side barrier gate and its immediate neighboring dot, $C_{BL(BR), \text{left(right)}}$; and the cross capacitance between each side barrier gate and the next neighbouring dot, $C_{\times BL(\times BR), \text{right(left)}}$. These results agree well with modelling performed using FastCap (see Table I). We note that by appropriate tuning of the barrier gate voltages, we are able to form approximately symmetric dots. With the relevant capacitances defined, we obtain the interaction energy between the two dots, using $E_m = (e^2/C_m)((C_{\Sigma, \text{left}} \cdot C_{\Sigma, \text{right}}/C_m^2) - 1)^{-1} \sim 500 \mu\text{eV}$ [22]. While the current structure enabled the formation of two nearly identical dots, our group is developing a multi (3) layer structure, where top-gates independently control the islands, a second layer of gates provides contacts to in-diffused source and drain, and a third layer provides the barrier gates. This structure allows the source and drain reservoirs to remain populated even for low electron numbers in the dots.

Figures 3(b,c) show fine scans of bias triangles at $V_{SD}=1.0$ mV and 0.5 mV respectively. Resonant tunneling through the ground state and excited states of the double dot is clearly observed in the high-resolution

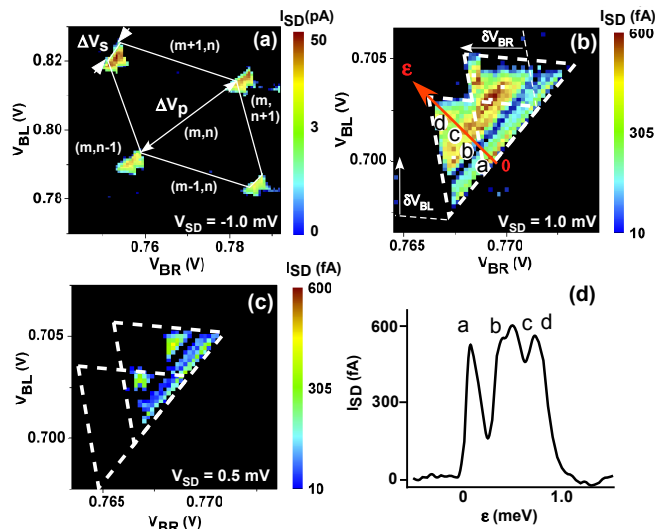


FIG. 3: Bias spectroscopy of a weakly coupled double dot with $V_{BM}=0.802$ V. (a) At finite source-drain bias, the triple points develop into triangle pairs. Relevant capacitances of the DQD can be extracted from the sizes of the hexagon and triangles. The fractional splitting, $F \sim 0.2$ indicates a dominant inter-dot capacitive coupling. (b, c) Detailed bias spectroscopy of a pair of triangles at $V_{SD}=1.0$ mV and 0.5 mV. (d) Line cut along the red arrow in (b) shows resonant tunneling through excited states in the transport.

TABLE I: Comparison of experimental values obtained from Fig. 3(a) and modelled FastCap capacitances. For definitions, see text.

		Experimental	FastCap
		Left(Right)	Modeling
$C_{\Sigma, \text{left(right)}}$	(aF)	22.8(26.4)	30.0
$C_{BL(BR), \text{left(right)}}$	(aF)	5.7(5.5)	5.3
$C_{\times BL(\times BR), \text{right(left)}}$	(aF)	0.75(0.90)	0.71
C_m	(aF)	1.9	1.5

bias-spectroscopy. With increasing V_{SD} , the triangular conducting regions become larger with more discrete levels in the bias window and the overlap of the triangle pairs increases. Figure 3(d) shows a plot of I_{SD} as a function of detuning energy, ϵ [23] between levels of the double dot. This I_{SD} line trace is extracted from a cut of the bias triangle as shown in Fig. 3(b), where the ground and excited state resonances are indicated by the labels *a-d*. The energy splitting of the first excited state *b* to its ground state *a* is $\sim 300 \mu\text{eV}$. We roughly estimate the average energy-level spacing of a dot via Weyl's formula, $\Delta E = 2\pi\hbar^2/gm^*A$, where A is the area of the dot. For a 2DEG system in Si, the effective mass of the electrons $m^*=0.19m_e$ and the degeneracy $g=4$, taking into account the spin and valley degeneracies [24]. Using this

we calculate $\Delta E \sim 400 \mu\text{eV}$, which would be the expected average level spacing if all symmetries are broken. Since no field is applied to the dots, the spacing would be a factor of 2 larger or $\sim 800 \mu\text{eV}$. In Fig. (d), we monitor transport through a serial configuration of two dots along the line cut presented in (b). In this case, we move the energy levels in both dots in opposite direction with respect to each other [2] with results in an effective reduction of a factor of two in the experimentally expected level splitting, in good agreement with the experimental data.

In conclusion, we have presented a tunable double-gated DQD defined in intrinsic silicon. The fabrication of the device is reproducible and MOS-compatible, enabling scale-up or integration into more complex designs. Transport measurements have been performed and extracted device capacitances were in good agreement with FastCap modelling. High resolution bias spectroscopy of the double dot presented evidence of resonant tunneling through ground and excited states, indicating that the system was in the few-electron regime. To reduce the electron number to a single electron in each dot we propose the incorporation of additional plunger gates, independently controlling each dot, together with an integrated charge detector [6] to monitor the dot occupancies. Such Si-based double quantum dot structures would have excellent potential for the investigation of the singlet-triplet two-level system due the long spin-coherence times in silicon.

The authors thank D. Barber and R.P. Starrett for technical support in the National Magnet Laboratory at UNSW, E. Gauja for the assistance in the UNSW Semiconductor Nanofabrication Facility, C.C. Escott, K.W. Chan and H. Yang for the help with the Fast-Cap modeling, and M.A. Eriksson, F.A. Zwanenburg and L.D. Macks for helpful comments with the manuscript. This work was supported by the Australian Research Council, the Australian Government, and by the U.S. National Security Agency (NSA) and U.S. Army Research Office (ARO) (under Contract No. W911NF-04-1-0290).

-
- [1] I.H. Chan, P. Fallahi, A. Vidan, R.M. Westervelt, M. Hanson, and A.C. Gossard, *Nanotechnology* **15**, 609 (2004).
 [2] W.G. van der Wiel, S. De Franceschi, J.M. Elzerman, T. Fujisawa, S. Tarucha, and L.P. Kouwenhoven, *Rev. Mod. Phys.* **75**, 1 (2002).
 [3] D. Loss and D.P. DiVincenzo, *Phys. Rev. A* **57**, 120

- (1998).
 [4] J.R. Petta, A.C. Johnson, J.M. Taylor, E.A. Laird, A. Yacoby, M.D. Lukin, C.M. Marcus, M.P. Hanson, and A.C. Gossard, *Science* **309**, 2180 (2005).
 [5] F.H.L. Koppens, C. Buizert, K.J. Tielrooij, I.T. Vink, K.C. Nowack, T. Meunier, L.P. Kouwenhoven, and L.M.K. Vandersypen, *Nature* **442**, 766 (2006).
 [6] D.J. Reilly, J.M. Taylor, J.R. Petta, C.M. Marcus, M.P. Hanson, and A.C. Gossard, *Science* **321**, 817 (2008).
 [7] C. Tahan, M. Friesen, and R. Joynt, *Phys. Rev. B* **66**, 035314 (2002).
 [8] A.M. Tyryshkin, J.J.L. Morton, S.C. Benjamin, A. Ardavan, G.A.D. Briggs, J.W. Ager, and S.A. Lyon, *J. Phys.: Condens. Matter* **18**, S783 (2006).
 [9] S.D. Lee, S.J. Shin, S.J. Choi, J.J. Lee, J.B. Choi, S. Park, S.-R.E. Yang, S.J. Lee, and T.H. Zyung, *Appl. Phys. Lett.* **89**, 023111 (2006).
 [10] S.J. Shin, J.J. Lee, R.S. Chung, M.S. Kim, E.S. Park, J.B. Choi, N.S. Kim, K.H. Park, S.D. Lee, N. Kim, and J.H. Kim, *Appl. Phys. Lett.* **91**, 053114 (2007).
 [11] H.W. Liu, T. Fujisawa, Y. Ono, H. Inokawa, A. Fujisawa, K. Takashina, and Y. Hirayama, *Phys. Rev. B* **77**, 073310 (2008).
 [12] H. Liu, T. Fujisawa, H. Inokawa, Y. Ono, A. Fujisawa, K. Takashina, and Y. Hirayama, *Appl. Phys. Lett.* **92**, 222104 (2008).
 [13] N. Shaji, C.B. Simmons, M. Thalakulam, L.J. Klein, H. Qin, H. Luo, D.E. Savage, M.G. Lagally, A.J. Rimberg, R. Joynt, M. Friesen, R.H. Blick, S.N. Coppersmith, and M.A. Eriksson, *Nature* **4**, 540 (2008).
 [14] S.J. Angus, A.J. Ferguson, A.S. Dzurak, and R.G. Clark, *Nano Lett.* **7**, 7 (2007).
 [15] S.J. Angus, A.J. Ferguson, A.S. Dzurak, and R.G. Clark, *Appl. Phys. Lett.* **92**, 112103 (2008).
 [16] K. Nabors and J. White, *IEEE Trans. Comput.-Aided Des.* **10**, 1447 (1991).
 [17] C.P. Heij, P. Hadley, and J.E. Mooij, *Appl. Phys. Lett.* **78**, 1140 (2001).
 [18] J.C. McCallum, M.L. Dunn, and E. Gauja, *Mater. Res. Soc. Symp. Proc.* **1074**, (2008).
 [19] D.R. McCamey, Ph.D. Thesis, The University of New South Wales, Sydney, Australia, (2007).
 [20] S. De Franceschi, S. Sasaki, J.M. Elzerman, W.G. van der Wiel, S. Tarucha, and L.P. Kouwenhoven, *Phys. Rev. Lett.* **86**, 878 (2001).
 [21] F.R. Waugh, M.J. Berry, D.J. Mar, R.M. Westervelt, K.L. Campman, and A.C. Gossard, *Phys. Rev. Lett.* **75**, 705 (1995).
 [22] N. Mason, M.J. Biercuk, and C.M. Marcus, *Science* **303**, 655 (2004).
 [23] Using formula $\alpha_L |e| \delta V_{BL} = \alpha_R |e| \delta V_{BR} = |\epsilon|$ [2], we calculate alpha factors $\alpha_L = 0.17$ ($\alpha_R = 0.19$), where δV_{BL} and δV_{BR} are defined in fig. 3(b).
 [24] D. Abusch-Magder, F. Simmel, D.A. Wharam, M.A. Kastner, and J.P. Kotthaus, *Physica E* **6**, 382 (2000).